RSC Advances

PAPER

View Article Online
View Journal | View Issue

Cite this: *RSC Adv.*, 2026, **16**, 23314

Pt–Y supported on magnesium–aluminium composite oxide catalysts for highly selective synthesis of 1,2-pentanediol from furfuryl alcohol under mild conditions

Xiaodong Zhou,[ab] Fengqin Guo,[b] Ziqiang Han,[bc] Jiajun Zhang,[bc] Yan Cao,[bc] Huiquan Li,[bc] Guozhu Chen *[a] and Liguo Wang *[bc]

The selective hydrogenolysis of furfuryl alcohol (FFA) to 1,2-pentanediol (1,2-PeD) represents a promising route for biomass valorization, yet it remains challenging due to the competing over-hydrogenation of the furan ring and the recalcitrant C_5–O bond cleavage. Herein, we report a highly efficient bimetallic Pt–Y catalyst supported on a MgO–AlO(OH) mixed oxide (MAO) that enables the selective hydrogenolysis of FFA to 1,2-PeD under remarkably mild conditions (140 °C, 0.8 MPa H_2). Structural characterizations (AC-HAADF-STEM, XPS) confirm the formation of Pt–Y mixed clusters, which induce electron transfer from Pt to Y. This electronic modulation, combined with the tailored basicity of the MAO support, effectively suppresses the over-hydrogenation pathway while promoting the activation of the target C–O bond. *In situ* Fourier transform infrared spectroscopy shows that after the introduction of Y, FFA adsorbs on the catalyst surface in a vertical adsorption configuration through its O–H and C–O–C bonds, promoting the selective ring-opening. Consequently, the optimized 0.75Pt0.45Y/MAO catalyst achieves complete FFA conversion with an exceptional 1,2-PeD selectivity of 80.3% (110 mol 1,2-PeD·mol Pt per h), significantly outperforming its monometallic counterparts. Furthermore, the catalyst demonstrates outstanding stability in a continuous-flow reactor for over 200 hours without obvious deactivation. This work provides a strategy for designing synergistic bimetallic catalysts for the sustainable production of 1,2-PeD under mild conditions.

Received 18th March 2026
Accepted 30th April 2026

DOI: 10.1039/d6ra02263d

rsc.li/rsc-advances

1 Introduction

The catalytic valorisation of biomass into high-value chemicals represents a pivotal and growing research frontier in sustainable chemistry.[1–3] Furfuryl alcohol (FFA), as an important biomass platform molecule, can be efficiently produced through the acid-catalysed hydrolysis of agricultural and forestry waste (such as corn cobs, sugarcane bagasse, *etc.*) and subsequent reduction reactions.[4,5] Furthermore, it can be converted into various downstream products through selective hydrogenation or hydrogenolysis, including 1,5-PeD, tetrahydrofurfuryl alcohol (THFOL), 1,2-PeD, 2-pentanol (2-PeOH), 1-pentanol (1-PeOH), and other high-value chemicals.[6,7] Among these, the selective hydrogenation of furfuryl alcohol to produce 1,2-pentanediol (1,2-PeD) has attracted significant attention due to its broad application prospects. 1,2-Pentanediol is an important polyol compound widely used in pharmaceutical intermediates, high-performance polymer monomers, and environmentally friendly solvents. It is a key industrial raw material in the manufacturing processes of polyester fibres and surfactants.[8,9] However, traditional production processes typically rely on multi-step oxidation or hydrolysis reactions of petroleum-based feedstocks, suffering from high energy consumption and low atom economy.[10] Therefore, developing efficient catalyst based on biomass derivatives for the green synthesis of 1,2-pentanediol holds significant scientific importance and industrial value.[11,12]

As early as the 1930s, the $CuCr_2O_4$ catalyst system was proven to exhibit catalytic activity for the direct hydrogenolysis of furfural/furfuryl alcohol (FA/FFA) compounds to produce pentanediols. However, the environmental pollution issue associated with chromium in this system significantly conflicts with contemporary green chemistry principles. To overcome this technical bottleneck, significant progress has been made in recent years in developing new catalytic systems: Zhang *et al.*[13] reported a Ru/MnO_x catalyst with basic sites as active sites for the hydrogenolysis of FFA to 1,2-PeD at 150 °C and

[a]*School of Chemistry and Chemical Engineering, University of Jinan, Jinan, 250022, China. E-mail: chm_chengz@ujn.edu.cn*

[b]*National Engineering Research Centre of Green Recycling for Strategic Metal Resources, Institute of Process Engineering, Chinese Academy of Science, Beijing, 100190, China. E-mail: lgwang@ipe.ac.cn*

[c]*School of Chemical Engineering, University of Chinese Academy of Sciences, Beijing, 100049, China*

1.5 MPa H_2 pressure, achieving 89.2% FFA conversion. However, the yield of 1,2-PeD was only 42.1%, and its catalytic stability and target product yield still need improvement. Kaneda *et al.*[8] reported complete conversion of FA and 73% selectivity to 1,2-PeD catalysed by Pt/hydrotalcite (HT) at 150 °C and 3 MPa. Wang *et al.*[14] studied the structure-performance relationship of platinum catalysts supported on CeO_2. Under conditions of 165 °C and 2 MPa H_2 pressure for 24 hours, Pt/CeO_2-C exhibited the best catalytic performance: achieving complete conversion of furfural (FFA) and 77% selectivity towards the target product 1,2-pentanediol (1,2-PeD). This study revealed the important regulatory role of support crystal facet engineering on the hydrogenolysis performance of noble metal catalysts. Later, D.S. Pisal *et al.*[15] reported complete FFA conversion and a high 1,2-PeD yield of 87% catalysed by a 1% Rh/OMS-2 catalyst at 160 °C and 3 MPa H_2, representing the best result reported to date. In the development of non-noble metal systems, researchers have constructed alternative solution represented by copper-based catalysts, but their harsh reaction conditions and 1,2-pentanediol selectivity below 55% are difficult to meet industrial demands.[16–19] Notably, current catalytic systems often rely on high-pressure hydrogen environments. This technical challenge has prompted the design and development of novel catalytic systems—specifically, the creation of catalysts that exhibit excellent catalytic performance under mild reaction conditions while maintaining a low loading of precious metals.

The selective hydrogenolysis of furfuryl alcohol (FFA) to 1,2-pentanediol (1,2-PeD) involves the cleavage of the C–O bond in the furan ring, which is typically facilitated by the presence of an unsaturated C=C bond adjacent to the oxygen atom. This unsaturation is crucial for the activation and ring-opening of the furan ring under mild conditions. However, a major competing reaction is the hydrogenation of the furan ring to form tetrahydrofurfuryl alcohol (THFA), which saturates the C=C bonds and results in a fully hydrogenated, stable cyclic ether structure. Once THFA is formed, the C–O bond within the saturated ring becomes significantly more resistant to cleavage, making subsequent ring-opening to 1,2-PeD virtually impossible under the same mild reaction conditions. Therefore, suppressing the formation of THFA is essential to preserve the integrity of the C=C bond, which serves as a key structural feature for facilitating the targeted C–O bond cleavage and ensuring high selectivity toward 1,2-PeD.[20] Previous reports have indicated that the adsorption configuration of furfuryl alcohol on the catalyst is crucial for selectivity.[5,21] Introducing a second metal as a promoter can modulate the electronic structure of the noble metal and create dual active sites.:[22,23] the noble metal site is responsible for hydrogen activation, while the promoter site enhances C–O bond adsorption and activation capability. For instance, Liu *et al.*[24] developed Pt/Ca co-modified nitrogen-doped carbon catalysts (*x*PtCa@CN) for the conversion of furfural (FA) to 1,2-pentanediol (1,2-PeD). Furthermore, previous reports have indicated that introducing transition metals benefit the adsorption of oxygen-containing groups and altering adsorption configurations due to the oxophilicity of transition metal cations.[25–27] This demonstrates the effectiveness of the bimetallic strategy in promoting C–O hydrocracking of biomass-derived molecules and enhancing the effectiveness of selectivity through the regulation of adsorption configurations.

In this study, we attempted to introduce the transition metal Y into the catalyst to construct a new catalytic system Pt–Y/MAO (MAO refers to a mixture of magnesium oxide and basic aluminium oxide, which is used to provide a moderately strong alkaline environment). Yttrium (Y) was chosen as a promoter due to its strong oxophilicity, which enhances the adsorption of oxygen-containing groups in furfuryl alcohol (FFA) and facilitates C–O bond activation. The MgO–AlO(OH) (MAO) support, on the other hand, offers moderately basic sites that promote O–H bond activation and hydrogen transfer, while the presence of AlO(OH) modulates the surface basicity to avoid excessive side reactions. The high surface area of MAO also ensures good dispersion of Pt–Y clusters. Together, these features are anticipated to direct FFA adsorption into a vertical configuration, favouring ring-opening over ring hydrogenation. It can catalyse the FA/FFA hydrogenolysis reaction under mild conditions as low as 0.8 MPa hydrogen pressure and 140 °C, providing up to 80.3% selectivity for 1,2-PeD, and it is capable of achieving a production rate of up to 110 $mol_{1,2\text{-PeD}}$ per mol_{Pt} per h under highly selective conditions. The use of biomass-derived feedstock, green solvent (water), mild reaction conditions, and a recyclable solid catalyst make this process sustainable and environmentally friendly.

2 Experimental

2.1 Catalyst synthesis

Preparation of MAO support. MAO support was prepared using the ball milling method. Specifically, light magnesium oxide and basic aluminium oxide were first mixed at a Mg : Al molar ratio of 3 : 1 and ball-milled at 800 rpm for 8 h. The resulting mixture was then calcined in a muffle furnace at 500 °C for 4 h. The MAO support was synthesized *via* a mechanochemical ball milling method, achieving thorough mixing of MgO and AlO(OH). This approach enables the generation of materials with high specific surface area and enhances metal–support interactions. The mechanical forces during ball milling induce lattice defects and surface activation, promoting the formation of heterojunction structures and facilitating the subsequent anchoring of Pt–Y clusters.[28]

Preparation of Pt–Y/MAO catalysts. The Pt–Y/MAO catalysts were prepared by the impregnation method. 0.01 g of chloroplatinic acid hexahydrate ($H_2PtCl_6 \cdot 6H_2O$, Aladdin) and 0.01 g of yttrium nitrate hexahydrate ($Y(NO_3)_3 \cdot 6H_2O$, Aladdin) were dissolved in 2 g of water. Then, 0.5 g of MAO was added, and the mixture was left to stand for 12 hours. The resulting catalyst precursor was dried at 80 °C for 12 h and reduced in H_2 at 300 °C for 60 min. After cooling to room temperature in H_2, the 0.75 wt% Pt-0.45 wt% Y/MAO catalyst was obtained, denoted as 0.75Pt0.45Y/MAO. Catalysts with 0.75 wt% Pt/MAO and 0.45 wt% Y/MAO were also prepared using the same method. The actual loads of Pt and Y are determined by ICP (Table S1).

2.2. Characterizations of catalyst

The crystal structure was characterized by wide-angle X-ray diffraction (XRD) using a PANalytical Empyrean multi-functional diffractometer equipped with a Cu Kα radiation source (40 kV, 40 mA). The XRD patterns were collected over a 2θ range of 5–90° with a scanning rate of 10° min^{-1}.

High-Angle Annular Dark-Field Scanning Transmission Electron Microscopy (HAADF-STEM) images were obtained on a Thermo Fisher Talos F200S G2 instrument. Before imaging, passivated samples were ultrasonically dispersed in ethanol and then dropped onto copper TEM grids. Spherical aberration-corrected transmission electron microscopy (AC-HAADF-STEM) images were acquired using a JEM-ARM300F instrument. Prior to imaging, the sample was ultrasonically dispersed in ethanol and then deposited onto a copper grid for observation.

CO_2 temperature-programmed desorption (TPD) and H_2 TPD were performed on the same chemisorption apparatus used for CO_2 and H_2 chemisorption. Prior to the measurement, 50 mg of the calcined sample was pretreated in pure H_2 at 600 °C for 30 min, followed by a purge pretreatment under helium flow (50 mL min^{-1}) to eliminate interference from moisture adsorption and the hydroxyl structure in AlO(OH) on the catalyst surface. After cooling to 50 °C, the sample was saturated with a 10% H_2/Ar or CO_2/He gas mixture (50 mL min^{-1}) for 1 h. The gas flow was then switched to Ar or He (30–50 mL min^{-1}) for 1 h to remove weakly physically adsorbed H_2. Finally, desorption was carried out by heating to 700 °C at a ramp rate of 10 °C min^{-1} under Ar or He atmosphere, and the desorbed gas was detected by TCD.

Quasi-in situ X-ray Photoelectron Spectroscopy (XPS) was conducted on a Thermo Scientific K-Alpha spectrometer equipped with an Al Kα X-ray source. Before measurement, calcined samples were pre-reduced at 300 °C for 60 min and then transferred to the measurement chamber without exposure to air. The binding energies of Pt and Y were calibrated using the C 1s peak of adventitious carbon at 284.8 eV.

In situ Fourier Transform Infrared Spectroscopy (*In situ* FT-IR; Model: Mettler Toledo React IR 15) was used to characterize the interaction between the catalyst and reactants during the reaction and to monitor reaction intermediates and products. Infrared signals were acquired every 1 min using an N_2 detector and a 9.5 mm AgX fiber probe. For the FFA adsorption experiments, 50 mg of the pre-reduced catalyst powder was placed in the cell. It was first pretreated at 300 °C for 1 hour under a nitrogen flow (30 mL min^{-1}) to clean the surface. The gas flow was then switched to a continuous stream of H_2 saturated with FFA (introduced *via* a temperature-controlled bubbler), while background and adsorption spectra were collected. To investigate the temperature-dependent evolution of the adsorption configuration, a temperature-programmed process (heating rate: 2 °C min^{-1}) was initiated under maintained FFA/H_2 flow, allowing *in situ* monitoring of the dynamic changes in the infrared spectra.

2.3 Activity testing

The catalyst test was conducted in a 20 mL high-pressure autoclave. Typically, 50 mg of catalyst, 0.1 g of furfuryl alcohol, and 4 mL of water were added to the autoclave. After sealing, the reactor was purged with H_2 at least three times and then pressurized to the desired pressure. The reaction is carried out at the required temperature for the specified duration of hours with stirring at 500 rpm. After completion, the liquid product was separated by centrifugation and analysed using a gas chromatograph (Extend-C18) equipped with a flame ionization detector (FID) and an FFAP column, with biphenyl as the internal standard. The carbon balance for each reaction was calculated by comparing the total carbon in the products and residual furfuryl alcohol to the initial carbon in furfuryl alcohol. All liquid products were quantified by GC-FID using biphenyl as the internal standard. The carbon content of each compound was calculated based on its molecular formula.

The stability of the 0.75Pt0.45Y/MAO catalyst was investigated in a continuous flow fixed-bed reactor under the conditions of 140 °C and 0.8 MPa H_2 (Scheme 1). First, quartz wool was filled at the bottom of the stainless-steel tubular reactor (inner diameter 9 mm, length 370 mm), then 1 g of the catalyst was loaded into the middle of the stainless-steel tubular reactor, and finally quartz sand was filled at the top of the reactor. Subsequently, the catalyst was reduced at 300 °C under a hydrogen atmosphere of 30 mL min^{-1} for 60 minutes, and then cooled to 140 °C. A 2.5 wt% furfuryl alcohol aqueous solution was pumped into the reactor at a flow rate of 0.01 mL min^{-1} (LHSV = 0.15 h^{-1}), while hydrogen was introduced at a flow rate of 8 mL min^{-1} (GHSV = 171 h^{-1}). A portion of the liquid product was analysed using a gas chromatograph equipped with an FID detector and an FFAP column (Extend-C18), with biphenyl used as the internal standard.

The conversion of FFA, and the selectivity of 1,2-PeD are calculated as follows:

$$\text{Conv. of FFA} = \frac{n_{\text{initial}}(\text{FFA}) - n_{\text{residual}}(\text{FFA})}{n_{\text{initial}}(\text{FFA})} \times 100\% \quad (1)$$

$$\text{Sel. of } 1,2\text{-PeD} = \frac{n(1,2\text{-PeD})}{n_{\text{initial}}(\text{FFA}) \times \text{Conv. of (FFA)}} \times 100\% \quad (2)$$

Among them, n_{initial}(FFA) represents the molar amount of furfuryl alcohol before the reaction; n_{residual}(FFA) denotes the

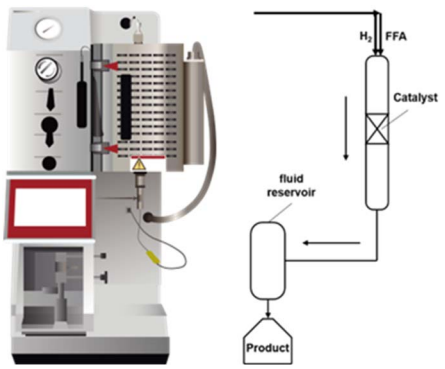

Scheme 1 Fixed-bed reactor schematic.

molar amount of furfuryl alcohol after the reaction; and n(1,2-PeD) is the molar amount of 1,2-pentanediol.

3. Results and discussion

3.1. Structural investigation

The Pt–Y/MAO series catalysts were characterized to obtain structural information. XRD patterns showed the characteristic peaks of the MAO support composed of mixed phases of MgO and AlO(OH) (Fig. S1). The absence of XRD peaks corresponding to Pt or Y/Y_2O_3 phases, and the lack of new peaks in the XRD patterns of the metal-loaded catalysts compared to the MAO support without impregnation, indicate high dispersion of both components. Although a slight shift of the XRD peaks toward lower angles was observed after metal loading, incorporation of Y into the AlO(OH) lattice is unlikely, as such doping typically requires temperatures above 1100 °C, far exceeding our synthesis conditions.[29,30] The reason may be that a small amount of Pt enters the near-surface lattice positions in the form of single atoms (Fig. S2), inducing local lattice expansion, which shifts the XRD diffraction peaks to lower angles. Regarding the decrease in peak width, we attribute this phenomenon to the grain growth of the support caused by heating during the reduction process of the catalyst. Subsequently, SEM characterization was conducted on the catalyst surface (Fig. S3). By comparing the morphologies of MAO and Pt–Y-MAO catalysts, it was found that they were basically the same, indicating that the impregnation method for loading metals does not significantly affect the surface morphology of the catalyst. The HAADF-STEM and HRTEM images of the 0.75 Pt/MAO and 0.75Pt0.45Y/MAO catalysts are shown in Fig. 1a and b. The results reveal that the MgO and AlO(OH) components are homogeneously mixed in both catalysts, with distinct lattice fringes from different phases clearly observable, exhibiting clear boundaries and close interconnection. The same phenomenon was also observed in the AC-HAADF-STEM image in Fig. 1c. The uniform distribution of Mg and Al elements also indicates that MgO and AlO(OH) are in close contact (Fig. 1f). These results provide sufficient evidence for the successful preparation of the heterojunction structure.[31] The nanoparticles were evenly dispersed on the MAO support. The introduction of Y promoted nanoparticle growth (Fig. S4), suggesting a potential interaction between Pt and Y (Fig. 1d and e).

Furthermore, aberration-corrected STEM characterization provided atomic-scale insight into the morphology of the metal species (Fig. 1h). For the 0.75Pt0.45Y/MAO catalyst, the loaded metals were predominantly present as sub-nanometric clusters.

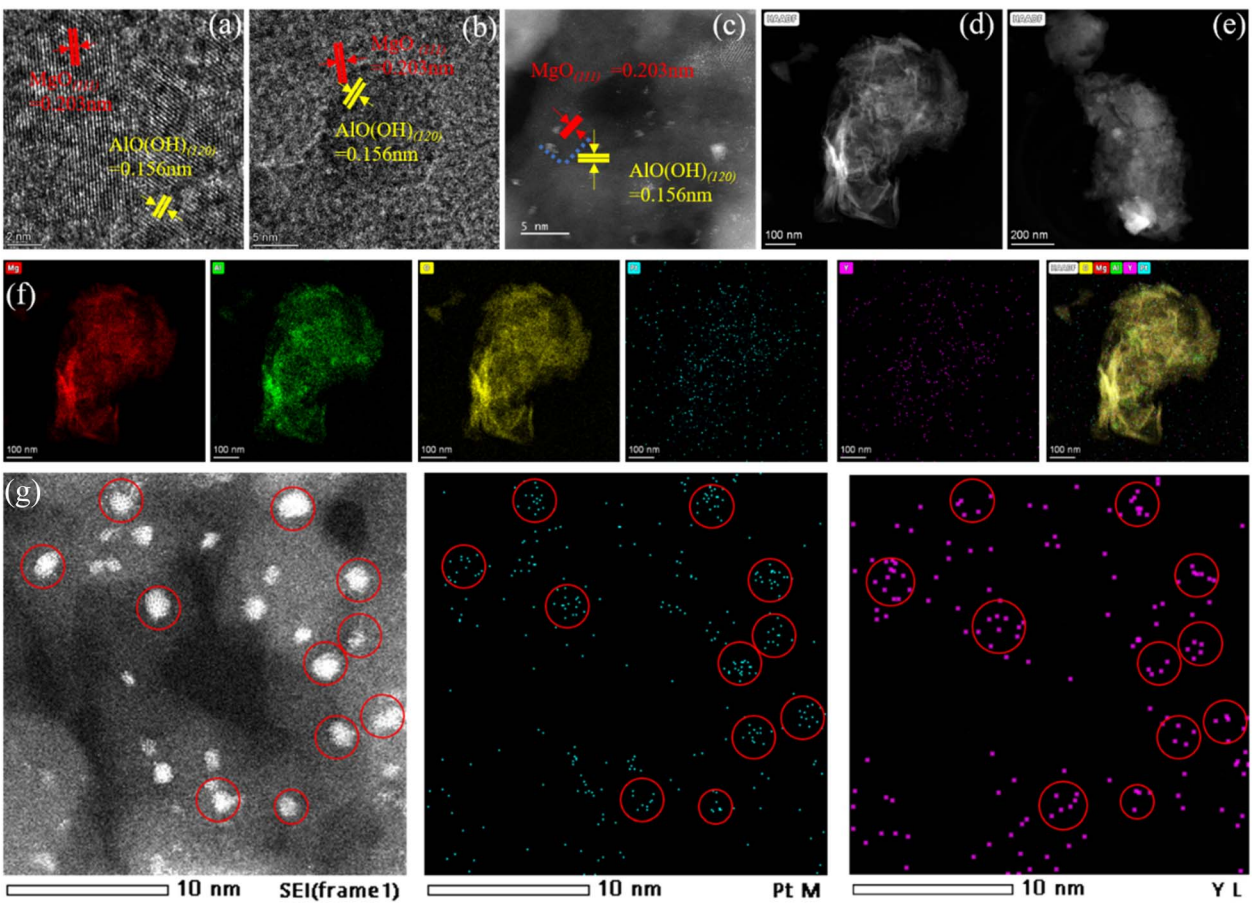

Fig. 1 (a) HRTEM images of MAO and (b) 0.75Pt-0.45Y/MAO catalysts; (c) AC-HAADF-STEM images of 0.75Pt-0.45Y/MAO catalysts; (d) HRTEM image of 0.75Pt-0.45Y/MAO and (e) 0.75 Pt/MAO catalyst; (f and g) elemental mapping image of 0.75Pt0.45Y/MAO catalyst.

The co-localization of Pt and Y signals within the same clusters, as observed in elemental mapping, provides definitive evidence for their direct interaction.

3.2. The surface properties investigation

H_2-TPD characterization was performed to evaluate the H_2 activation capability of the MAO series catalysts (Fig. 2a). Corresponding to adsorbed hydrogen on the catalyst. As shown in Fig. 2a, the Pt-loaded sample exhibited the highest hydrogen adsorption capacity (431 μmol H_2 g_{cat}^{-1}). After the introduction of the Y component, the hydrogen adsorption capacity decreased (196 μmol H_2 g_{cat}^{-1}). Similarly, a comparable phenomenon was observed in CO_2-TPD (Fig. 2b). The total base amount of the 0.75Pt0.45Y/MAO catalyst is 4.02 mmol g^{-1}, which is significantly lower than that of the 0.75 Pt/MAO catalyst (6.56 mmol g^{-1}). This can be explained by the significant weakening of H_2 chemisorption due to the strong electronic interaction between Pt and Y. Similar phenomena have been observed previously in other systems.[22,32,33] Fig. 2c presents the CO_2-TPD profiles of the catalyst supports with different Mg/Al ratios, with a detailed discussion provided in the following section. As shown in Fig. S5, H_2 uptake increased with Pt loading due to more surface Pt atoms. The desorption temperature rose slightly at higher loadings, indicating a weaker electronic effect from Y as the Y/Pt ratio decreased. The optimal 0.75Pt-0.45Y/MAO catalyst shows balanced H_2 uptake and Pt–H strength, enabling selective C–O cleavage while suppressing ring hydrogenation. In contrast, lower Pt loading limits activity, while higher loading promotes Pt-like behaviour and increases ring hydrogenation risk.

The electronic properties of Pt and Y in these Pt–Y/MAO catalysts were characterized by XPS. Although a portion of the Pt signal overlaps with the Al signal, a slight protrusion corresponding to the Pt$4f_{7/2}$ component is observed.[34] As shown in Fig. S6, for the freshly reduced 0.75 Pt/MAO catalyst, the Pt $4f_{7/2}$ binding energy was centred at 71.2 eV, indicating Pt is primarily in the metallic state (Pt^0).[35] In comparison, the Pt $4f_{7/2}$ peak binding energy for the 0.75Pt0.45Y/MAO catalyst was 71.6 eV, suggesting electron transfer from Pt to Y. On the other hand, Y 3d XPS showed that for the 0.8Pt0.4Y/MAO catalyst (Fig. 2e), the Y $3d_{3/2}$ binding energy was 156.2 eV, indicating a Y^{3+} valence state.[36] While the Y $3d_{3/2}$ binding energy of the 0.45Y/MAO catalyst is centred at 156.6 eV, suggests electron transfer from Pt to Y, proving the bonding of Pt and Y, which is consistent with the TEM results. To further confirm, we measured the Pt 4d region (Fig. 2d), which is free from signal overlap. The Pt 4d binding energy of 0.75Pt0.45Y/MAO is 0.4 eV higher than that of 0.75 Pt/MAO, consistent with the Pt 4f results and confirming electron transfer from Pt to Y. The interaction between Pt and Y was further evaluated by CO pulse measurement and CO-TPD experiments. As shown in Fig. 2f and Table S2, the CO uptake decreased significantly upon Y addition, from 12.19 μmol g^{-1} for 0.75 Pt/MAO to 9.51 μmol g^{-1} for 0.75Pt-0.45Y/MAO. Concomitantly, the CO desorption temperature in the CO-TPD profiles shifted downward by 50 °C (Fig. 2f), providing direct evidence for the electronic modification of Pt by Y. Furthermore, previous reports have indicated that the presence of low-valent transition metal cations favours the adsorption of oxygen-containing groups due to their oxyphilicity.[21–23] Therefore, it can be anticipated that the bonding of Y^{3+} with metallic Pt will facilitate the selective cleavage of the C–O bond on FFA.

3.3. Catalytic performance

The performance of materials for converting FFA to 1,2-PeD was evaluated (Fig. 3a). The conversion efficiency of FFA on MAO

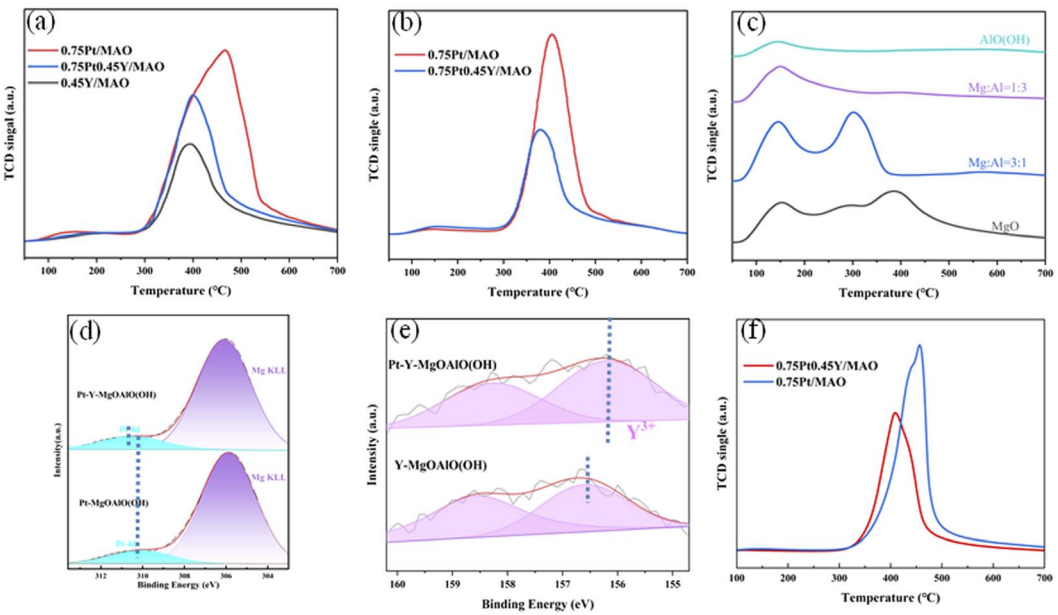

Fig. 2 (a and b) H_2-TPD and CO_2-TPD results for 0.75Pt-0.45Y/MAO, 0.75 Pt/MAO, and 0.45Y/MAO catalysts,(c) CO_2-TPD results for catalyst supporters with different Mg : Al molar ratios (d and e) XPS spectra of Pt 4d and Y 3d on different Pt–Y/MAO catalysts, (f) CO-TPD results for 0.75Pt-0.45Y/MAO, 0.75 Pt/MAO.

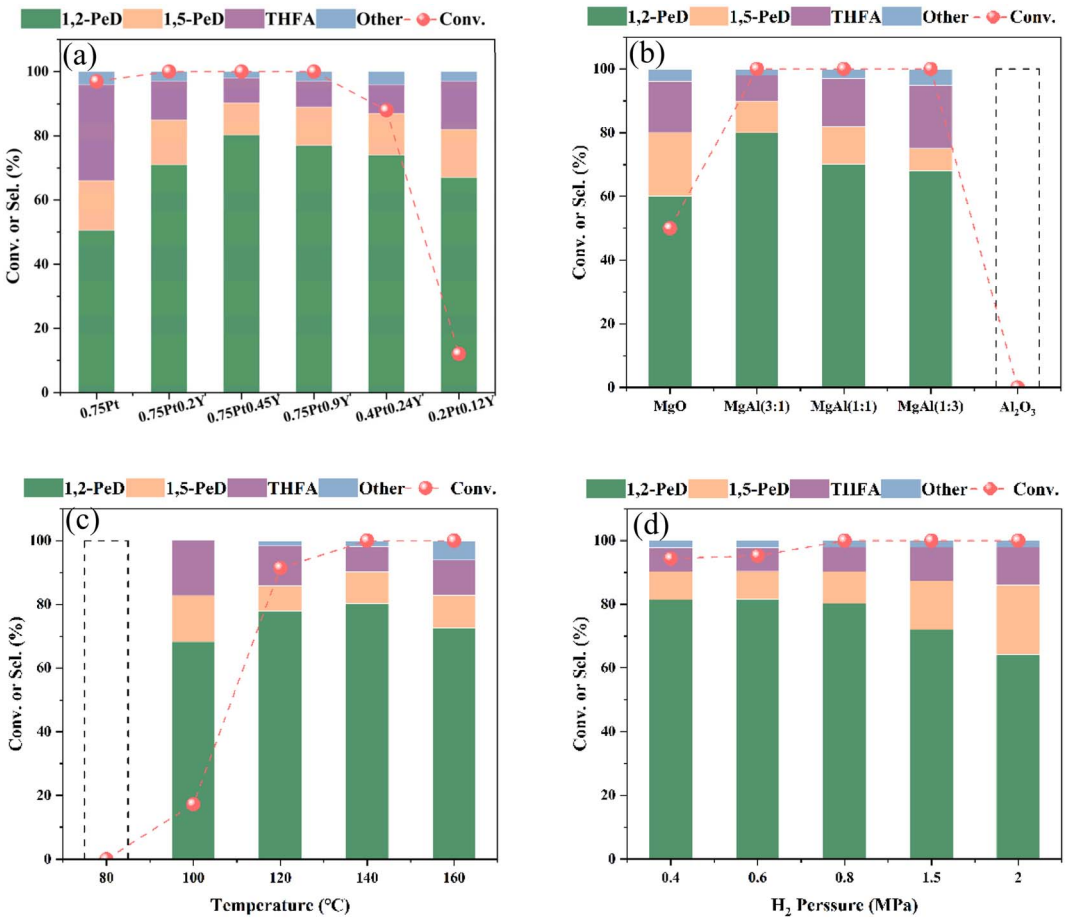

Fig. 3 (a) Hydrogenation reactions of MAO catalysts for different loadable substances; (b) hydrogenation reaction over Pt–Y/MAO catalysts with different Mg and Al ratios. (c) Hydrogenation reaction on 0.75Pt0.45Y/MAO catalyst at different temperatures. Re action conditions: 4 mL H_2O, 0.1 g FFA, 50 mg catalyst, 0.8 MPa H_2, 6 h; (d) hydrogenation reaction on 0.75Pt0.45Y/MAO catalyst at different pressures. Reaction conditions: 4 mL H_2O, 0.1 g FFA, 50 mg catalyst, 140 °C, 6 h.

alone was very low. Similarly, Y/MAO also showed very low conversion efficiency. On the other hand, Pt/MAO catalyst exhibits high hydrogenation activity and achieves complete FFA conversion after six hours of reaction, simultaneously, the selectivity towards THFA was 31%, indicating that furan ring hydrogenation predominated, with a small portion undergoing cleavage reactions. To improve ring-opening selectivity, ring hydrogenation must be suppressed because once THFA is formed, this ring is difficult to cleave (Table S3). When a second component Y is present in the catalyst, even in very small amounts, THFA formation is greatly inhibited, and selectivity increases. Specifically, in order to compare the selectivity of 1,2-PeD after complete conversion, after the reaction lasted for six hours, the 0.75Pt0.45Y/MAO catalyst achieved 80.3% selectivity for 1,2-PeD, while hydrogenation byproducts including FFA and 1-butanol (1-BuOH) were marginal. This performance represents a significant improvement over the vast majority of those reported in the literature (Table 1). Among the Pt–Y/MAO catalysts mentioned above, the best-performing catalyst (0.75Pt0.45Y/MAO) had a Y/Pt atomic ratio of 1.67. We then investigated the influence of Pt content by fixing the Y/Pt ratio at 1.67, aiming to maximize Pt atomic efficiency. Pleasingly, when the Pt content was reduced from 0.75% to 0.4%, the 1,2-PeD selectivity only slightly decreased from 80.3% to 74%. When the Pt content was reduced to an extremely low value of 0.2%, the catalyst still maintained high selectivity towards ring-opening, achieving 82%, and although FFA conversion was only 12%, the 1,2-PeD selectivity hardly decreased, remaining above 65%. Previously, Shao *et al.* reported a selectivity of 63.9% for 1,2-PeD over a 2% Pt/Mg_7AlO catalyst.[18] Compared to that result, our Pt–Y/MAO clearly provides higher ring-opening selectivity and higher Pt metal efficiency. This demonstrates the significant promoting effect of Y. As revealed by XPS analysis, electron transfer from Pt to Y, thereby inhibiting ring hydrogenation on Pt sites. Therefore, the introduction of Y as a promoter should be the reason for the greatly improved ring-opening selectivity.

Previous research has indicated that water is involved in hydrogen transfer during the reaction, which in turn facilitates the ring-opening pathway.[37] We have proved through experiments that there can be rapid proton exchange between water and the substrate (Fig. S7). And MgO can also promote the activation of water in the reaction.[38] To investigate the influence of different Mg : Al molar ratios on reaction performance, the effect of Pt–Y/MAO catalysts on the selective hydrogenation of

Table 1 Catalytic performances of the different catalysts for furfuryl alcohol hydrogenolysis comparison with the literature on the production rate of 1,2-PeD by hydrogenolysis of FA or FFA over noble metal catalyst

Feedstock	Catalyst	Conditions	Conversion (%)	Selectivity (%)		Ref.
				1,2-PeD	1,5-PeD	
FFA	4Ru/MnO_x	150 °C 1.5 MPa 6 h	89.2	41.4	—	13
FFA	10Ru/Al_2O_3	200 °C 10 MPa 1 h	100	32.0	—	40
FFA	1Ru-5Sn/ZnO	140 °C 3.5 MPa 6 h	100	84.5	9.2	41
FFA	5Ru/MgO	190 °C 3 MPa 1 h	100	42.0	2.9	42
FA	20Ru/PVP	125 °C 2 MPa 48 h	100	36.0	—	43
FA	3Pd/MMT-K	220 °C 3.5 MPa 5 h	>99.0	66.0	—	44
FFA	4.5Pt/CeO_2	165 °C 2 MPa 24 h	49.8	77.1	7.3	45
FFA	0.8Pt0.4Fe/MT	140 °C 1 MPa 15 h	100	75.0	20.0	23
FFA	0.75Pt0.45Y/MAO	140 °C 0.8 MPa 6 h	100	80.3	10.0	This work

FFA to 1,2-PeD was studied. The results are shown in Fig. 3b. As the Mg : Al molar ratio decreased, the yield of 1,2-PeD initially increased and then decreased. The presence of acidic and basic sites has a significant impact on catalytic activity.[39] When the support consisted only of AlO(OH), FFA conversion was almost negligible. This might be because AlO(OH), although possessing basic sites, has weak basic strength and may lack sufficient metal-support interaction, leading to insufficient electron density on Pt/AlO(OH) and rendering it unable to activate furfuryl alcohol or intermediates. Secondly, when the support was MgO, the reaction was incomplete and selectivity was low (50%). This is because MgO has strong basicity, which can promote FFA activation through dehydrogenation or hydrogenolysis involving the C=O bond. However, its excessive basicity may lead to over-hydrogenation, generating the byproduct THFA. Additionally, pure MgO has a low specific surface area and poor dispersion of active sites, resulting in insufficient conversion.[46] For mixed supports, complete FFA conversion was achieved across different ratios. This might be because when MgO is mixed with AlO(OH), the weak basicity of AlO(OH) neutralizes the strong basicity of MgO, forming moderate basic strength that can activate FFA while avoiding excessive reaction. Simultaneously, the acidic sites of AlO(OH) are suppressed by MgO, reducing side reactions, this can also be demonstrated by conducting CO_2-TPD tests on catalyst supporter with different Mg : Al molar ratios (Fig. 2c). Moreover, the strong electron-donating effect of MgO can modulate the electron density of Pt, promoting H_2 dissociation and hydrogen transfer; while the high specific surface area of AlO(OH) improves the dispersion of Pt–Y particles, increasing the number of active sites. The combination places Pt–Y in an optimal electronic state, favouring the selective formation of 1,2-PeD. The highest 1,2-PeD yield (80.3%) was obtained at the optimal Mg/Al ratio (3 : 1). At this ratio, basic sites on the support surface (from MgO) dominate but are not excessive, ensuring initial FFA activation; a small amount of AlO(OH) (25%) provides sufficient dispersion and weak acidic sites, stabilizing reaction intermediates and reducing excessive side reactions.

The selectivity of FFA to 1,2-PeD over the 0.75Pt0.45Y/MAO catalyst at different reaction temperatures was studied (Fig. 3c). Below 120 °C, although the main product was 1,2-PeD, the reactants were not completely converted, indicating that FFA hydrogenolysis and ring-opening proceed smoothly. As the reaction temperature increased from 120 °C to 160 °C, the yield of 1,2-PeD significantly increased. Correspondingly, more alcohols (1,5-PeD and 1-BuOH) were formed. The selectivity of 1,2-PeD increased from 68.3% at 100 °C to 80.3% at 140 °C, while further increasing to 160 °C resulted in a 1,2-PeD yield of 72.5%. The byproduct 1-BuOH was not detected at reaction temperatures below 100 °C. As the reaction temperature continued to increase, the 1-BuOH yield increased from 2% to 6%, indicating that higher temperatures promote 1-BuOH formation, possibly due to the partial conversion of 1,2-PeD route to 1-BuOH. The conversion of FFA to 1,2-PeD over the 0.75Pt0.45Y/MAO catalyst under different hydrogen pressures was further investigated (Fig. 3d). As shown, FFA was completely converted even at 0.8 MPa H_2 pressure, proving H_2 saturation. However, when pressure was further increased to 2 MPa, it was found that excessive pressure promotes the formation of 1,5-PeD. This is likely because the high-pressure environment facilitates the cleavage of the C_1–O bond, leading to this phenomenon.

3.4. Reaction kinetics and mechanism

Since the adsorption configuration of furan ring compounds plays an important role in the hydrogenation pathway and product selectivity.[47,48] FT-IR spectroscopy of FFA was conducted to investigate the adsorption configuration of FFA on the catalyst surface and elucidate the mechanism of FFA conversion to 1,2-PeD. First, the adsorption of FFA on the Pt–Y/MAO catalyst at different temperatures was compared (Fig. 4a). Characteristic peaks at 1149, 1038, and 1320 cm^{-1} were assigned to the C–O–C and C=C bonds of FFA adsorbed on the Pt–Y/MAO catalyst.[49] It indicates that the O atom in the furan ring adsorb onto the active sites of Pt–Y/MAO. When the temperature was increased from 30 °C to 180 °C, it could be observed that at low temperatures, only the characteristic peak for the C–O–C bond was present, demonstrating that low temperatures are not favourable for the adsorption of the C=C bond. However, as the temperature gradually increased, the characteristic peak for the C=C bond gradually appeared at 1320 cm^{-1}. This indicates the emergence of a new adsorption configuration for the C=C bond

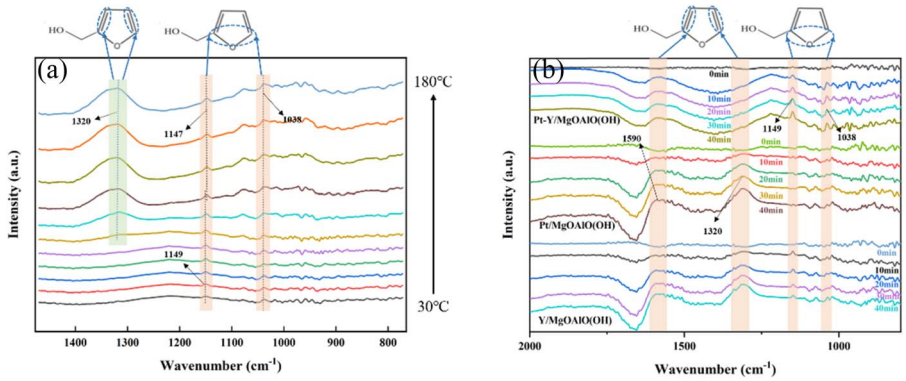

Fig. 4 Adsorption configurations represented by FT-IR: (a) FFA on 0.75Pt0.45Y/MAO at different temperatures; (b) FFA on different catalysts.

on the catalyst, signifying that increased temperature leads to more ring hydrogenation reactions, and indeed, previous experiments have confirmed this.

Subsequently, the adsorption of FFA on different catalysts was compared (Fig. 4b). The characteristic peaks at 1590 and 1320 cm^{-1} were assigned to the adsorption of the C=C bond of FFA on the Pt–Y/MAO catalyst, while the peaks at 1149 and 1038 cm^{-1} were attributed to the adsorption of the C–O–C bond. First, regarding C–O–C bond adsorption, near 1147 cm^{-1}, almost no adsorption peak of the C–O–C bond was observed on Pt/MAO compared to Pt–Y/MAO and Y/MAO. This demonstrates that introducing the Y component significantly enhances the catalyst's adsorption toward the C–O–C bond in the furan ring of the substrate. Moreover, for the adsorption of the C=C bond of FFA, distinct adsorption peaks corresponding to the C=C bond were observed at 1590 cm^{-1} on both Pt–Y/MAO and Y/MAO, whereas the adsorption peak on Pt–Y/MAO was notably weak. This indicates that the coexistence of Pt and Y strongly suppresses the tilted adsorption configuration of the C=C bond of FFA on the catalyst surface—a configuration generally favourable for furan ring hydrogenation. Taken together, in the Pt–Y bimetallic system, the introduction of Y enhances adsorption toward the substrate's C–O–C bond, while the synergistic effect of Pt and Y weakens adsorption toward the C=C bond in the furan ring. This results in FFA maintaining an upright orientation on the catalyst surface. Such an adsorption configuration on Pt–Y/MAO strongly promotes the ring-opening reaction of the furan ring, which also explains why more ring hydrogenation reactions occur on the Pt/MAO catalyst.

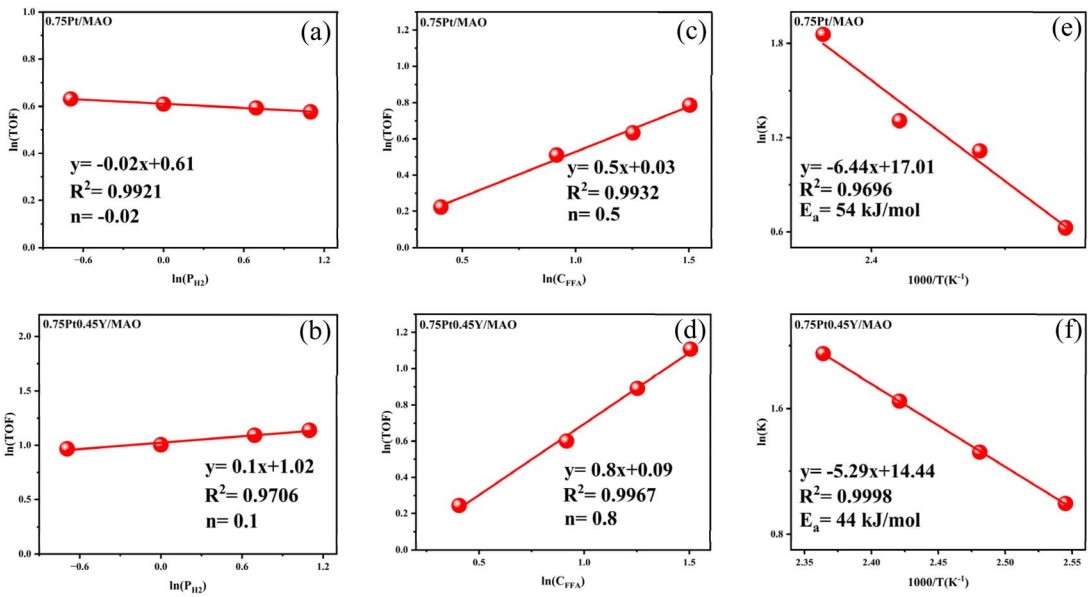

Fig. 5 The reaction rate with respect to hydrogen pressure and FFA concentration over (a and c) 0.75 Pt/MAO and (b and d) 0.75Pt0.45Y/MAO catalysts. Reaction conditions: 50 mg of 0.75 Pt/MAO or 50 mg of 0.75Pt0.45Y/MAO catalyst, 140 °C. For the hydrogen pressure effect: 0.1 g of FFA in 4 g of water, P_{H_2}: 0.5, 1, 2, 3 MPa; for the FFA concentration effect: 4 g of water, 1 MPa H_2, CFFA: 1.5%, 2.5%, 3.5%, 4.5%. Arrhenius plots for the FFA hydrogenolysis reaction over the (e) 0.75 Pt/MAO and (f) 0.75Pt0.45Y/MAO catalysts. Reaction conditions: 0.1 g of FFA in 4 g of water, 1 MPa H_2, 50 mg of 0.75 Pt/MAO, temperature range of 120–150 °C or 50 mg of 0.75Pt0.45Y/MAO, temperature range of 120–150 °C TOF = FFA μmol per min per molPt.

To systematically evaluate the impact of yttrium modification on the kinetic behaviour of platinum-based catalysts in the ring-opening reaction, this study employed furfuryl alcohol (FFA) as a probe molecule to comparatively investigate the reaction performance of 0.8 Pt/MAO and 0.8Pt0.4Y/MAO (Y/Pt atomic ratio = 1.67) catalysts (Fig. 5). The experiments were conducted within a hydrogen pressure range of 0.5–3 MPa, and intrinsic kinetic parameters were obtained by monitoring the FFA conversion process. The results show that both catalysts exhibit zero-order reactions in the hydrogen reaction rate. Suggesting that the surface of the active sites was nearly saturated with hydrogen under the given conditions, and hydrogen activation was not the rate-determining step.

Concurrently, the reaction orders with respect to FFA were 0.5 and 0.8 for the two catalysts, respectively, reflecting competitive adsorption behaviour of FFA on the catalyst surface and indicating that the adsorption and activation processes of FFA are partially involved in the rate-determining step of the reaction. Furthermore, the apparent activation energy measured for the 0.8 Pt/MAO catalyst was 54 kJ mol^{-1}, while that for the 0.8Pt0.4Y/MAO catalyst decreased to 44 kJ mol^{-1}. This difference further indicates that the incorporation of yttrium not only alters the energy barrier heights along the reaction pathway but may also induce a restructuring of the electronic structure or local coordination environment of the active sites. Consequently, it influences the adsorption modes of reactant molecules and the reaction mechanism, thereby promoting the reaction.

Before calculations, MgO(100)/AlOOH(010) lateral structure (MgO(100)/AlOOH(010)-ls) was constructed based on MgO conventional standard cell (JCPDS #04-001-7295) and AlOOH conventional standard cell (JCPDS #98-000-0120). Furthermore, in the previous experiments, we found that using only AlO(OH) to load Pt–Y clusters had no catalytic effect at all. Therefore, we built $Pt_4Y_2O_3$ on MgO and constructed the MgO(100)/AlOOH(010)-ls-$Pt_4Y_2O_3$ cluster model. In slab model, thickness along *c* direction was set at 30 Å to avoid weak interactions between image. Adsorption energy of molecule on slab model was determined by E_{ads}. $E_{ads} = E_{(AB)} - E_{(A)} - E_{(B)}$. $E_{(AB)}$ represents the total energy of slab model A with molecule B adsorbed on surface. $E_{(A)}$ represents the total energy of slab model A. $E_{(B)}$ represents the total energy of molecule B in its gas phase. In this case, configurations of furfuryl alcohol were optimized in a 20 × 20 × 20 $Å^{-3}$ cell box, respectively.

As shown in Fig. 6, FFA exhibits the highest adsorption energy on Pt–Y/MAO, while the adsorption energy decreases on Pt/MAO. In this work, all calculations were carried out through the Vienna *Ab initio* Simulation Package (VASP) with the projector augmented wave (PAW) method. The Perdew–Burke–Ernzerhof (PBE) functional with the generalized gradient approximation (GGA) method was used to do with the exchange–correlation functional, in combination with the DFT-D3 correction. The cut-off energy of the plane-wave basis is set at 450 eV. For optimization of geometry of slab model, the Brillouin Zone integration was performed with a Monkhorst–Pack5 *k*-point mesh of 1 × 2 × 1. The self-consistent calculations apply a convergence energy threshold of 10^{-5} eV, and the

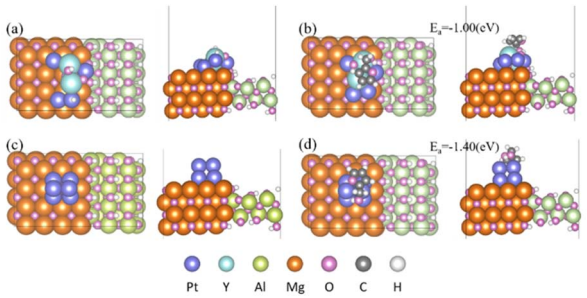

Fig. 6 (a and c) Model construction of Pt/MAO and Pt–Y/MAO; (b and d) Adsorption energy of FFA on Pt/MAO and Pt–Y/MAO.

equilibrium geometries are optimized with maximum stress on each atom within 0.02 eV $Å^{-1}$. Spin polarization method was adopted to describe magnetism of slab models. For the adsorption reaction of molecules, the energy is calculated through the following equations:

$$E_{ad} = E_{surface+absorbate} - E_{surface} - E_{absorbate}$$

where $E_{surface+adsorbate}$ is the total energy of adsorption model, $E_{surface}$ is the total energy of surface and $E_{adsorbate}$ is the total energy of adsorbate. Combined with previous results from *in situ* diffuse reflectance infrared spectroscopy, these findings indicate that the introduction of Y species enables organic molecules to interact strongly with sites on the Y_2O_3 surface *via* their oxygen atoms, while simultaneously interacting with Pt metal sites through their carbon rings or carbon chains. This dual-functional adsorption mode is considerably stronger than mere physical/chemical adsorption on Pt alone. Such an adsorption configuration facilitates the cleavage of the C–O bond in the ring, thereby promoting the progression of the reaction.

Based on the above experimental results and previous literature, a possible reaction mechanism for FFA conversion to 1,2-PeD on the Pt–Y/MAO catalyst is proposed (Fig. 7). First, the O–H bond of FFA and the C–O–C bond on the furan ring adsorb onto the catalyst support surface and the Y site in the supported metal, respectively. Simultaneously, H_2 dissociates into two H atoms on the Pt surface. The dissociated H atoms are activated by basic sites. Then, H attacks the carbon atom at the C_5–O bond, leading to furan ring opening. Subsequently, the dissociated hydrogen reduces the remaining C=C bond to generate 1,2-PeD.

3.5. Stability

Besides activity and selectivity, catalyst stability is another crucial performance indicator, particularly important for practical applications. In most previous studies, the reaction from FFA to pentanediol was conducted in batch reactors.[44,50] Limiting the assessment of long-term catalyst stability. In this work, based on catalyst screening, we further evaluated the long-term operation of the 0.75Pt0.4Y/MAO catalyst in a continuous fixed-bed reactor. Moreover, we maintained the conversion rate at 90% by controlling the amount of the

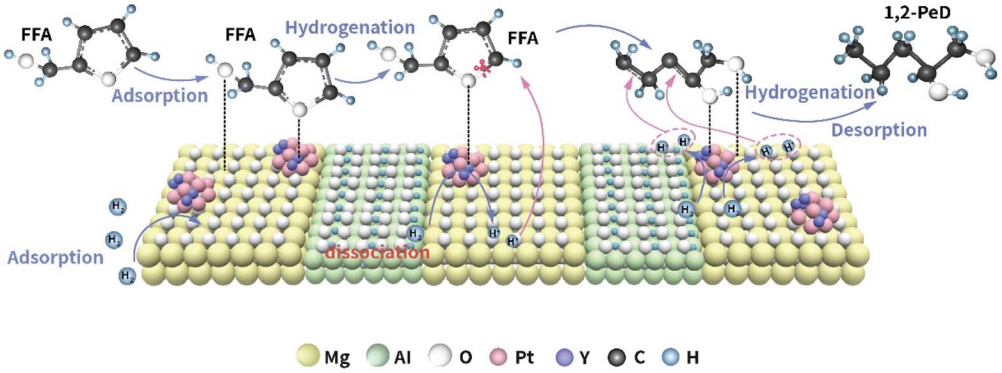

Fig. 7 Plausible reaction pathway for FFA conversion to 1,2-PeD.

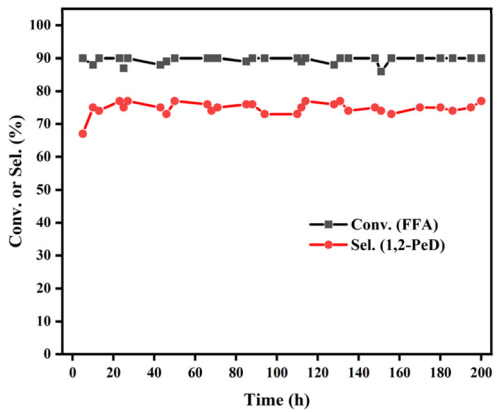

Fig. 8 Long-term stability test of the 0.75Pt0.45Y/MAO catalyst. Reaction conditions: 140 °C, 0.8 MPa H_2; liquid flow rate: 0.01 mL min^{-1}; gas flow rate: 8 mL min^{-1}; 2.5 wt% FFA aqueous solution, 1 g catalyst.

catalyst, thereby proving that the catalyst was not used in excess. (Table S5).[51] The results are shown in Fig. 8. The catalyst performed quite stably over a 200-hour runtime. The XPS analysis of the used catalysts revealed that the oxidation states of Pt and Y remained unchanged after the reaction (Fig. S11). The HAADF-STEM images of the used catalysts (Fig. S12) showed that the Pt–Y nanoparticles were still highly dispersed and there was no obvious sintering, indicating that the nanostructure of the active sites was not disrupted during the long-term reaction.

4. Conclusions

In summary, we have successfully developed a bimetallic Pt–Y/MAO catalyst for the highly selective hydrogenolysis of biomass-derived furfuryl alcohol to 1,2-pentanediol under mild reaction conditions. The key to the superior performance lies in the synergistic interplay between Pt and Y. Detailed characterization revealed that Y coexists with Pt in the form of intimately associated clusters, facilitating electron transfer from Pt to Y. This electronic engineering, coupled with the modulated surface basicity of the MgO–AlO(OH) support, plays a dual role: it effectively suppresses the undesired over-hydrogenation of the furan ring and concurrently enhances the adsorption and activation of the critical C_5–O bond. *In situ* spectroscopic studies further elucidated that this synergy promotes a vertical adsorption mode of FFA, directing the reaction pathway toward selective ring-opening. The optimized catalyst achieves a remarkable 1,2-PeD selectivity of 80.3% at complete conversion, alongside demonstrating excellent long-term stability. This study not only presents a highly active and stable catalyst for biomass upgrading but also offers fundamental insights into the design principle of bimetallic catalysts, where promoter metals can tune both electronic properties and reactant adsorption configurations to achieve precise selectivity control in complex reaction networks. The strategy underscores the potential of utilizing non-precious promoters to enhance the efficiency and sustainability of noble metal-catalysed biomass conversion processes.

Author contributions

Xiaodong Zhou: original draft, investigation, validation, data curation. Fengqin Guo: investigation, validation. Ziqiang Han: investigation, validation. Jiajun Zhang: resources, supervision. Yan Cao: resources, supervision. Huiquan Li: supervision, funding acquisition. Guozhu Chen: writing – review, supervision. Liguo Wang: conceptualization, writing – review & editing, supervision, funding acquisition.

Conflicts of interest

The authors declare that they have no known competing financial interests or personal relationships that could have appeared to influence the work reported in this paper.

Data availability

The authors declare that the data supporting the findings of this study are available within the paper and its supplementary information (SI) files. Should any raw data files be needed in another format they are available from the corresponding author upon reasonable request. Source data are provided with this paper. Supplementary information: Fig. S1: XRD patterns of

the series of MAO, Y/MAO, Pt/MAO, Pt–Y/MAO catalysts; Fig. S2: AC-HAADF-STEM images of 0.75Pt-0.45Y/MAO catalysts; Fig. S3: (a and c)SEM images of MAO and (b and d) 0.75Pt-0.45Y/MAO catalysts; Fig. S4: particle size statistics on 0.75 Pt/MAO (a) and 0.75Pt-0.45Y/MAO (b) catalysts; Fig. S5: The H_2-TPD results of catalyst carriers with different Pt loading amounts; Fig. S6: TOF values under different reaction pressure over 0.75 Pt/MAO and 0.75Pt0.45Y/MAO catalysts. Reaction conditions: 50 mg of 0.75 Pt/MAO or 50 mg of 0.75Pt0.45Y/MAO catalyst, 140 °C. For the hydrogen pressure effect: 0.1 g of FFA in 4 g of water, P_{H_2}: 0.5, 1, 2, 3 MPa; Fig. S7: TOF values under different FFA concentration over 0.75 Pt/MAO and 0.75Pt0.45Y/MAO catalysts. Reaction conditions: 50 mg of 0.75 Pt/MAO or 50 mg of 0.75Pt0.45Y/MAO catalyst, 4 g of water, 1 MPa H_2, CFFA: 1.5%, 2.5%, 3.5%, 4.5%; Fig. S8: TOF values under different temperature over 0.75 Pt/MAO and 0.75Pt0.45Y/MAO catalysts. Reaction conditions: 0.1 g of FFA in 4 g of water, 1 MPa H_2, 50 mg of 0.75 Pt/MAO, temperature range of 120–150 °C or 50 mg of 0.75Pt0.45Y/MAO, temperature range of 120–150 °C; Table S1: the amount of Pt and Y in the impregnation solution; Table S2: basic physical-chemical properties of different catalysts; Table S3: catalytic performance of the 0.75Pt0.45Y/MAO catalyst for the THFA hydrogenolysis; Table S4: carbon balance for FFA hydrogenolysis over 0.75Pt0.45Y/MAO catalyst; Table S5: comparison of conversion rates between catalyst in excess and catalyst in insufficient amount in a fixed-bed reactor. See DOI: https://doi.org/10.1039/d6ra02263d.

Acknowledgements

This work was financially supported by National Natural Science Foundation of China. (NSFC 22278409), The National Key R&D Program of China. (2022YFC3902200).

Notes and references

1 K. Lee, Y. Jing, Y. Wang and N. Yan, *Nat. Rev. Chem.*, 2022, **6**, 635–652.
2 R. Mariscal, P. Maireles-Torres, M. Ojeda, I. Sadaba and M. Lopez Granados, *Energy Environ. Sci.*, 2016, **9**, 1144–1189.
3 S. Wang, H. Li and M. Wu, *J. Clean. Prod.*, 2021, **303**, 126825.
4 Y. Liu, X. Huang, Z. Huang, F. Su and D. Song, *Appl. Catal., A*, 2026, **711**, 120754.
5 S. Dou, L. Ma, Y. Dong, Q. Zhu and X. Kong, *J. Colloid Interface Sci.*, 2024, **663**, 345–357.
6 K. Huang, Z. J. Brentzel, K. J. Barnett, J. A. Dumesic, G. W. Huber and C. T. Maravelias, *ACS Sustain. Chem. Eng.*, 2017, **5**, 4699–4706.
7 Z. Yu, N. Ji, J. Xiong, Y. Han, X. Li, R. Zhang, Y. Qiao, M. Zhang and X. Lu, *Small*, 2022, **18**, 2201361.
8 T. Mizugaki, T. Yamakawa, Y. Nagatsu, Z. Maeno, T. Mitsudome, K. Jitsukawa and K. Kaneda, *ACS Sustain. Chem. Eng.*, 2014, **2**, 2243–2247.
9 Y. Shi, Y. Zhu, Y. Yang, Y.-W. Li and H. Jiao, *ACS Catal.*, 2015, **5**, 4020–4032.
10 Y. Li, Y. Shen, J. Zhang, C. Chen, X. Zhang, B. Geng and G. Wang, *Fuel*, 2025, **387**, 134398.
11 R. Yangcheng, J. Li, J. He, Y. Zheng, H. Yu, C. Chen and J. Wang, *Small*, 2024, **20**, 2309821.
12 H. Yu, Y. Xu, K. Havener, M. Zhang, L. Zhang, W. Wu and K. Huang, *Small*, 2022, **18**, 2106893.
13 B. Zhang, Y. Zhu, G. Ding, H. Zheng and Y. Li, *Green Chem.*, 2012, **14**, 3402–3409.
14 T. Tong, X. Liu, Y. Guo, M. N. Banis, Y. Hu and Y. Wang, *J. Catal.*, 2018, **365**, 420–428.
15 D. S. Pisal and G. D. Yadav, *ACS Omega*, 2019, **4**, 1201–1214.
16 H. Liu, Z. Huang, F. Zhao, F. Cui, X. Li, C. Xia and J. Chen, *Catal. Sci. Technol.*, 2016, **6**, 668–671.
17 F. Gao, H. Liu, X. Hu, J. Chen, Z. Huang and C. Xia, *Chin. J. Catal.*, 2018, **39**, 1711–1723.
18 Y. Shao, J. Wang, H. Du, K. Sun, Z. Zhang, L. Zhang, Q. Li, S. Zhang, Q. Liu and X. Hu, *ACS Sustain. Chem. Eng.*, 2020, **8**, 5217–5228.
19 T. P. Sulmonetti, B. Hu, S. Lee, P. K. Agrawal and C. W. Jones, *ACS Sustain. Chem. Eng.*, 2017, **5**, 8959–8969.
20 Y. Nakagawa, M. Tamura and K. Tomishige, *ACS Catal.*, 2013, **3**, 2655–2668.
21 J. Wang, S. Zhu, Y. He, G. Fan, X. Li, X. Jia, M. Dong and W. Fan, *Catal. Today*, 2024, **433**, 114647.
22 B. Hu, Z. Li, B. Wang, L. Chen, X. Wang, X. Hu, Z. Bai, Y. Li, G. Chen, X. Luo and S.-F. Yin, *Appl. Catal. B Environ. Energy*, 2025, **371**, 125196.
23 C. Cao, W. Guan, Q. Liu, L. Li, Y. Su, F. Liu, A. Wang and T. Zhang, *Green Chem.*, 2024, **26**, 6511–6519.
24 H. Liu, Y. Qiu, R. Shan, J. Zhang, H. Yuan and Y. Chen, *J. Environ. Chem. Eng.*, 2025, **13**, 118125.
25 Y. Ren, Y. Tang, L. Zhang, X. Liu, L. Li, S. Miao, D. S. Su, A. Wang, J. Li and T. Zhang, *Nat. Commun.*, 2019, **10**, 4500.
26 Y. Zhang, L. Li, F. Liu, H. Qi, L. Zhang, W. Guan, Y. Liu, A. Wang and T. Zhang, *ACS Catal.*, 2022, **12**, 6302–6312.
27 Y. Zhang, F. Zhang, L. Li, H. Qi, Z. Yu, X. Liu, C. Cao, F. Liu, A. Wang and T. Zhang, *J. Catal.*, 2023, **417**, 301–313.
28 D. Leybo, K. L. Firestein, N. D. Evdokimenko, A. A. Ryzhova, V. S. Baidyshev, I. V. Chepkasov, Z. I. Popov, A. L. Kustov, A. S. Konopatsky, D. V. Golberg and D. V. Shtansky, *ACS Appl. Nano Mater.*, 2022, **5**, 16475–16488.
29 F. Nahif, S. Mráz, D. Music, P. Keuter and J. M. Schneider, *Surf. Coat. Technol.*, 2014, **257**, 333–337.
30 D. Xu, H. Jiang, M. Li, O. Hai and Y. Zhang, *Ceram. Int.*, 2015, **41**, 5355–5361.
31 X. Gong, Z. Fan, Y. Wang, X. Qiu, Y. Xie, Y. Ling and J. Zhao, *Appl. Catal., A*, 2023, **668**, 119470.
32 N. Lei, X. Zhao, B. Hou, M. Yang, M. Zhou, F. Liu, A. Wang and T. Zhang, *Chemcatchem*, 2019, **11**, 3903–3912.
33 N. Xi, Q. Li, Y. Chen, R. Bao, Q. Wang, Y. Lin, J. Yue, R. Wang, C. Yang, W. Yin and T. Qiu, *Chem. Eng. J.*, 2025, **512**, 162222.
34 J. Wang, S. Zhu, Z. Lv, X. Jia, X. Li, M. Dong and W. Fan, *Catal. Today*, 2025, **447**, 115145.
35 X. Jin, R. Tsukimura, T. Aihara, H. Miura, T. Shishido and K. Nozaki, *Nat. Catal.*, 2021, **4**, 312–321.
36 S. Damyanova, I. Shtereva, B. Pawelec, L. Mihaylov and J. L. G. Fierro, *Appl. Catal., B*, 2020, 278.
37 R. Ma, X.-P. Wu, T. Tong, Z.-J. Shao, Y. Wang, X. Liu, Q. Xia and X.-Q. Gong, *ACS Catal.*, 2017, **7**, 333–337.

38 M. Feng, Z. Chen, H. Sun, S. Yao, Z. Liu, M. Lu, F. Li, H. Wang and L. Liu, *J. Energy Chem.*, 2025, **107**, 582–590.
39 M. Zhang, C.-B. Hong, Z. Ding, Y. Weng, H. Gong, H. Wang, Y. Zhang, Y. Liao and H. Liu, *Chem. Eng. J.*, 2024, **502**, 158100.
40 D. Goetz, M. Lucas and P. Claus, *React. Chem. Eng.*, 2016, **1**, 161–164.
41 P. P. Upare, Y. Kim, K.-R. Oh, S. J. Han, S. K. Kim, D.-Y. Hong, M. Lee, P. Manjunathan, D. W. Hwang and Y. K. Hwang, *ACS Sustain. Chem. Eng.*, 2021, **9**, 17242–17253.
42 A. Yamaguchi, Y. Murakami, T. Imura and K. Wakita, *Chemistryopen*, 2021, **10**, 731–736.
43 L. Bruna, M. Cardona-Farreny, V. Colliere, K. Philippot and M. R. Axet, *Nanomaterials*, 2022, **12**, 328.
44 N. S. Date, R. C. Chikate, H.-S. Roh and C. V. Rode, *Catal. Today*, 2018, **309**, 195–201.
45 T. Tong, Q. Xia, X. Liu and Y. Wang, *Catal. Commun.*, 2017, **101**, 129–133.
46 V. Hiremath, B. T. Shiferraw and J. G. Seo, *J. CO2 Util.*, 2020, **42**, 101294.
47 X. Chen, W. Liu, J. Luo, H. Niu, R. Li and C. Liang, *Ind. Eng. Chem. Res.*, 2022, **61**, 12953–12965.
48 Z. Tong, X. Li, J. Dong, R. Gao, Q. Deng, J. Wang, Z. Zeng, J.-J. Zou and S. Deng, *ACS Catal.*, 2021, **11**, 6406–6415.
49 Y. Zhu, W. Zhao, J. Zhang, Z. An, X. Ma, Z. Zhang, Y. Jiang, L. Zheng, X. Shu, H. Song, X. Xiang and J. He, *ACS Catal.*, 2020, **10**, 8032–8041.
50 P. P. Upare, Y. Kim, K.-R. Oh, S. J. Han, S. K. Kim, D.-Y. Hong, M. Lee, P. Manjunathan, D. W. Hwang and Y. K. Hwang, *ACS Sustain. Chem. Eng.*, 2021, **9**, 17242–17253.
51 S. L. Scott, *ACS Catal.*, 2018, **8**, 8597–8599.